crystals

MDPI

Article

Study on Single-Layer and Single-Channel Microstructure of 304 Stainless Steel Using Joule Heat Additive Manufacturing

Suli Li [1,2,3,*], Zhuang Gao [1], Jie Xiong [1], Longfei Fan [1], Jichao Chen [1], Kaiyue Ma [1], Laixia Yang [1] and Bingheng Lu [2,3]

[1] School of Mechanical Engineering, Xi'an University of Science and Technology, Xi'an 710054, China; 21205016012@stu.xust.edu.cn (Z.G.); 21205016014@stu.xust.edu.cn (J.X.); 22205224130@stu.xust.edu.cn (L.F.); 22205224142@stu.xust.edu.cn (J.C.); 20205224136@stu.xust.edu.cn (K.M.); yanglx@xust.edu.cn (L.Y.)
[2] State Key Laboratory of Mechanical Manufacturing System Engineering, Xi'an Jiaotong University, Xi'an 710049, China; bhlu@mail.xjtu.edu.cn
[3] National Innovation Center for Additive Manufacturing, Xi'an 710100, China
* Correspondence: lsl15802949318@xust.edu.cn

Abstract: In this study, a solution to the issue of a large heat-affected zone in Wire Arc Additive Manufacturing is presented by employing the Joule Heat Additive Manufacturing method to create a single layer and single channel with a reduced heat-affected zone. The microstructure of the single layer and single channel is thoroughly investigated using various detection methods, including optical microscopy (OM), scanning electron microscopy (SEM), energy-dispersive spectroscopy (EDS), and electron backscatter diffraction (EBSD). The results reveal that the heat-affected zone formed by the Joule Heat Additive Manufacturing method is smaller than that produced by the Wire Arc Additive Manufacturing method. Additionally, the grains in the single layer and single channel progress from planar to columnar, then equiaxed, and finally back to columnar from the fusion line to the top of the wire. The element content and distribution are relatively uniform. The microstructure of the single layer consists of austenite and a small amount of ferrite, with austenite accounting for 99.71% of the content. The grain size in the middle of the wire is mainly around 10 μm, with the smallest angle grain boundaries within 10°. The distribution of local grain orientation differences in the three regions is found to be largely consistent. The analysis of the microstructure of the single layer and single channel serves as a valuable reference for understanding the behavior of single-channel multi-layers in future studies.

Keywords: additive manufacturing; 304 stainless steel; microstructure; Joule heat

Citation: Li, S.; Gao, Z.; Xiong, J.; Fan, L.; Chen, J.; Ma, K.; Yang, L.; Lu, B. Study on Single-Layer and Single-Channel Microstructure of 304 Stainless Steel Using Joule Heat Additive Manufacturing. *Crystals* **2023**, *13*, 1573. https://doi.org/10.3390/cryst13111573

Academic Editor: José L. García

Received: 19 September 2023
Revised: 24 October 2023
Accepted: 1 November 2023
Published: 7 November 2023

1. Introduction

Additive manufacturing (AM), also known as 3D printing, is a manufacturing technology in which 3D data models intended for manufacturing or repair are sliced layer by layer using professional software [1]. These slices are then stacked layer by layer based on the slice file, forming the object from the bottom up. Additive manufacturing technology has demonstrated significant value and wide-ranging applications in strategic emerging industries such as aerospace, rail transit, new energy, new materials, and medical instruments [2]. Currently, the mainstream metal-based additive manufacturing technologies include laser-based additive manufacturing (LMD) [3,4], electron beam additive manufacturing (EBAM) [5,6], and arc additive manufacturing (WAAM) [7]. However, these mainstream additive manufacturing methods suffer from low energy utilization and high manufacturing costs. To address these issues, scholars have recently proposed an innovative additive manufacturing method that utilizes Joule heat as the heat source [8,9]. This approach, known as Joule Heat Additive Manufacturing (JHAM), offers the benefits of closed-loop energy transfer, low energy consumption, and a simple equipment structure [10].

Different types of metal additive manufacturing methods, in the printing process, will show different physical and chemical changes in the material, and the properties of the samples formed will be different. The fundamental reason is that the evolution and distribution of material structure in the printing process determines its properties. Guo Tingbiao et al. [11] discovered that after a certain amount of extrusion, the Cu0.6Cr alloy exhibited a clear refinement in its structure and maintained a preferred orientation during the deformation process. As the number of extrusion passes increased, the alloy's tensile strength and hardness showed significant improvement. In a study by Lai Yongjun et al. [12], a prolonged homogenization heat treatment resulted in a notable reduction in element segregation. Additionally, the area and average size of the micropores continuously increased, followed by a first-time increase and then a decrease in micropore density. The size of the γ′ phase gradually increased, while the area fraction of the γ′ phase exhibited an initial increase and then a subsequent decrease. The durability of the alloy demonstrated an initial increase and then a decrease with the rise in primary aging temperature. Liu Liming et al. [13] studied the arc additive microstructure and properties of 316 stainless steel under different paths and found that the bottom, middle, and top microstructures of the specimen were mainly γ austenite, γ austenite, δ ferrite, and fine axial crystal, respectively, and the Vickers hardness first decreased and then increased from the bottom to the top. Rahul Unnikrishnan et al. [14] studied the effect of heat input on the microstructure of 304 stainless steel joints. Grain growth was observed near the fusion boundary, and austenite dendrites in the welding zone showed strong crystal orientation. The team of Yuan Chengwei [15] from Shandong University of Technology studied the electro-thermal mechanical response analysis of the plastic deformation of resistance-heated metal wire, and explored the plastic deformation of metal melt during the melting deposition forming process of resistance-heated metal wire. At present, the microstructure of a single-layer single channel formed by JHAM technology has not been analyzed, so it is necessary to characterize the grain structure.

In this paper, the JHAM method is employed to conduct an experiment on a 304 stainless steel single layer and single channel. The focus of this research is on the single layer and single channel formed under optimal process parameters. Additionally, we compare the heat-affected zone of the single layer and single channel formed using the arc additive manufacturing method. Furthermore, various detection methods are utilized to analyze the microstructure of different areas within the single-layer single-pass section.

2. Experimental Materials and Methods

2.1. Experimental Principles and Equipment

The principle of JHAM is shown in Figure 1. A programmable DC power supply is used to short-circuit the metal wire and the substrate. The electricity flows through the roller to the wire and the substrate in turn, the Joule heat generated by the wire itself is used to melt the wire, and the single-layer single-channel printing is realized by controlling the movement of the micro milling machine. The parameters selected in the experiment were determined according to the previous study of our research group [10]. The optimal shape was obtained when the dry elongation of the wire was 12 mm, the angle between the guide nozzle and the substrate was 30°, the vacuum was 7×10^{-2} Pa, the platform moving speed was 150 mm/min, the current was 260 A, the pressure was 0.60 N, and the contact length was 1.3 mm.

The experimental platform was designed and improved based on the CNC/M-1 (Xianhe Yuexin, Zibo, China) micro CNC milling machine. The specific parameters of the CNC/M-1 CNC milling machine and the programmable DC power supply IT-M3910D-10-1020 (ITECH, Nanjing, China) are shown in Table 1; the roller is the core component connected to the positive electrode of the power supply, and the pressure sensor is used to detect the function in the printing process. The maximum voltage and current provided are 10 V and 1020 A, respectively. The vacuum system mainly consists of the TRIVAC D60T (LEYBOLD, Cologne, Germany) mechanical pump, which can pump the atmospheric

pressure in the cabin to less than 10 Pa in 5 min, close the diverter valve, open the plunger valve, and then open the TURBOVAC 90 i (LEYBOLD, Cologne, Germany) semi-magnetic suspension molecular pump. The pressure in the test chamber can be pumped to 10-2 Pa within 15 min. The main performance parameters of the mechanical pump and the molecular pump are shown in Table 2. The entire vacuum system is equipped with a GRAPHIX (LEYBOLD, Cologne, Germany) high-precision vacuum gauge to accurately detect the actual vacuum inside the test chamber.

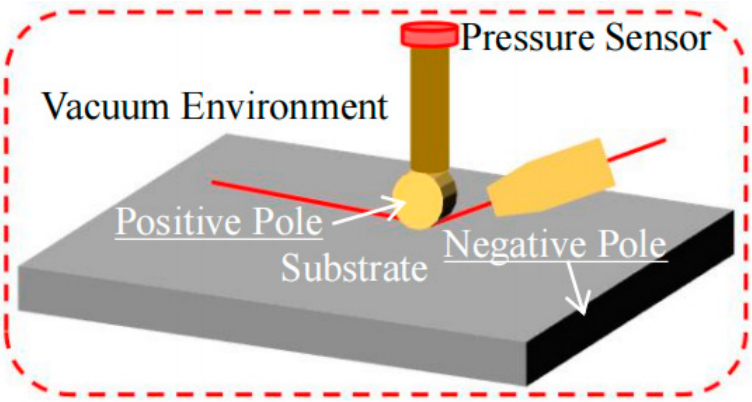

Figure 1. Principle of JHAM.

Table 1. Main parameters of CNC/M-1 CNC milling machine and IT-M3910d-10-1020 programmable DC power supply.

CNC Milling Machine	Parameter	Work Travel (mm × mm × mm)	Dimensions (mm × mm × mm)	Repeat Positioning Accuracy (mm)	Max. Moving Speed (mm/min)	Spindle Motor Power (kW)	Max. Spindle Speed (rpm)
	Value	90 × 65 × 65	380 × 240 × 410	±0.002	5000	0.1	3000
Power Supply	Parameter	Dimensions (mm × mm × mm)	Voltage Range (V)	Current Range (A)	Output Power Range (kW)	Power Supply Regulation Rate (%)	Setting Accuracy (%)
	Value	435 × 640 × 85	0~10	0~1020	0~10.2	≤0.01	≤0.02

Table 2. Main parameters of molecular pump and mechanical pump.

Parameter		**Pumping Speed (L/s)**	**Gas Throughput (L/s)**	**Compression Ratio (mm)**	**Rotational Speed (rpm)**	**Maximum Foreline Pressure (mbar)**	**Ultimate Pressure (mbar)**	**Weight (kg)**
Value	90i Molecular Pump	435 × 640 × 85	0~10	0~1020	0~10.2	≤0.01	≤0.02	≤2
	D60T Mechanical Pump	17.5	\	\	1400	\	0.3	70

2.2. Experimental Materials

In this experiment, 304 stainless steel wire with a diameter of 0.3 mm and a 316 L stainless steel round plate with a thickness of 5 mm and a diameter of 120 mm were selected for the substrate. The chemical composition of the two materials is shown in Table 3, and the physical properties at room temperature (20 °C) are shown in Table 4 [16,17]. The calculation formula of the electrical resistivity (ρ) is shown in Formula (1), where l represents the length of the wire, S represents the cross-sectional area of the wire, and R represents the

resistance of the wire. The calculation formula of thermal conductivity Q is shown in Formula (2), where Q represents the heat conduction through the wire, d represents the length of the wire, A represents the cross-sectional area of the wire, and ΔT represents the temperature difference of the wire. Where the electrical resistivity usually increases with the increase in temperature, this is due to the fact that the electrons in the metal increase the collision frequency when heated, and the resistance increases. Thermal conductivity usually increases with temperature. This is because at high temperatures, the vibrations of atoms and electrons increase, making heat conduction more efficient.

$$\rho = \frac{RS}{l} \tag{1}$$

$$Q = -\mathrm{k} \times \mathrm{A} \times \frac{\Delta T}{\mathrm{d}} \tag{2}$$

Table 3. Chemical composition of 304 and 316 L stainless steel (mass fraction/%).

Material	Fe	Cr	Mn	Mo	Ni	Si	C	P	S
304	69.34	18.01	0.77	0.03	8.03	0.47	0.052	0.027	0.003
316 L	68.33	16.38	0.86	2.11	10.11	0.44	0.018	0.026	0.007

Table 4. Physical properties of 304 and 316 L stainless steel (20 °C).

Material	Density (g/cm^3)	Specific Heat Capacity (kJ/kg·°C)	Melting Point (°C)	Thermal Conductivity (W/m·°C)	Electrical Resistivity ($\Omega \cdot mm^2/m$)
304	7.93	0.50	1400	14.63	0.73
316 L	7.98	0.502	1400	13.31	0.74

This experiment has high requirements for the surface quality of the substrate. In order to ensure the repeatability of process parameters and reduce errors, the stainless steel substrate was treated as follows before printing: The NC milled semi-finished stainless steel substrate was polished with 800 mesh sandpaper and 1200 mesh sandpaper, respectively. After being rinsed with water and sprayed with industrial alcohol, the substrate and wire were wiped with oil-free paper and dried with a hair dryer to remove machining marks and dirt on the surface and ensure that the surface of the substrate was smooth and clean.

2.3. Detection Method

The experimental results of the single-layer single channel were obtained using wire-cutting technology, as depicted in Figure 2a. After sample preparation, including rough grinding, fine grinding, and polishing, the surface was treated with Kalling solution for corrosion. Subsequently, the samples were washed and dried with anhydrous ethanol promptly. The cross-section morphology and microstructure of the single-layer single channel were then observed.

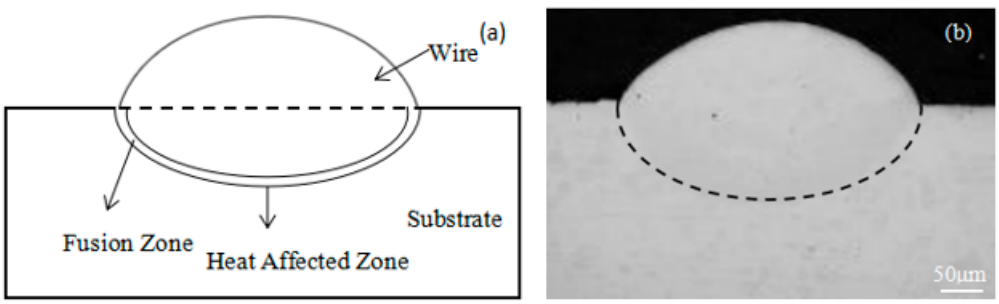

Figure 2. Geometric schematic diagram (**a**) and actual fusion diagram (**b**) of the single layer and single channel.

For the observation of the actual fusion cross-section of a single layer, Figure 2b displays the results captured under an optical microscope. The microstructure of the single layer was observed using an AX10 optical microscope from ZEISS, Oberkochen, Germany. Furthermore, the element composition and distribution of the single layer were analyzed using a JSMIT500 tungsten filament scanning electron microscope from JEOL, Tokyo, Japan. Additionally, the morphology of the single-channel grain was observed through EBSD measurements conducted on a JSM-7900 field emission scanning electron microscope equipped with an EBSD probe.

3. Results and Analysis

3.1. Microstructure Analysis of Single Layer and Single Channel

The microstructure observed in each region of the single-channel section under the optical microscope is illustrated in Figure 3. In Figure 3a,b, we can observe the original microstructure of the wire and substrate, both mainly composed of austenite grains with equal axes, although their shapes differ. This discrepancy arises because the wire and substrate undergo distinct cold drawing and forging processes, influencing the size and shape of the grains.

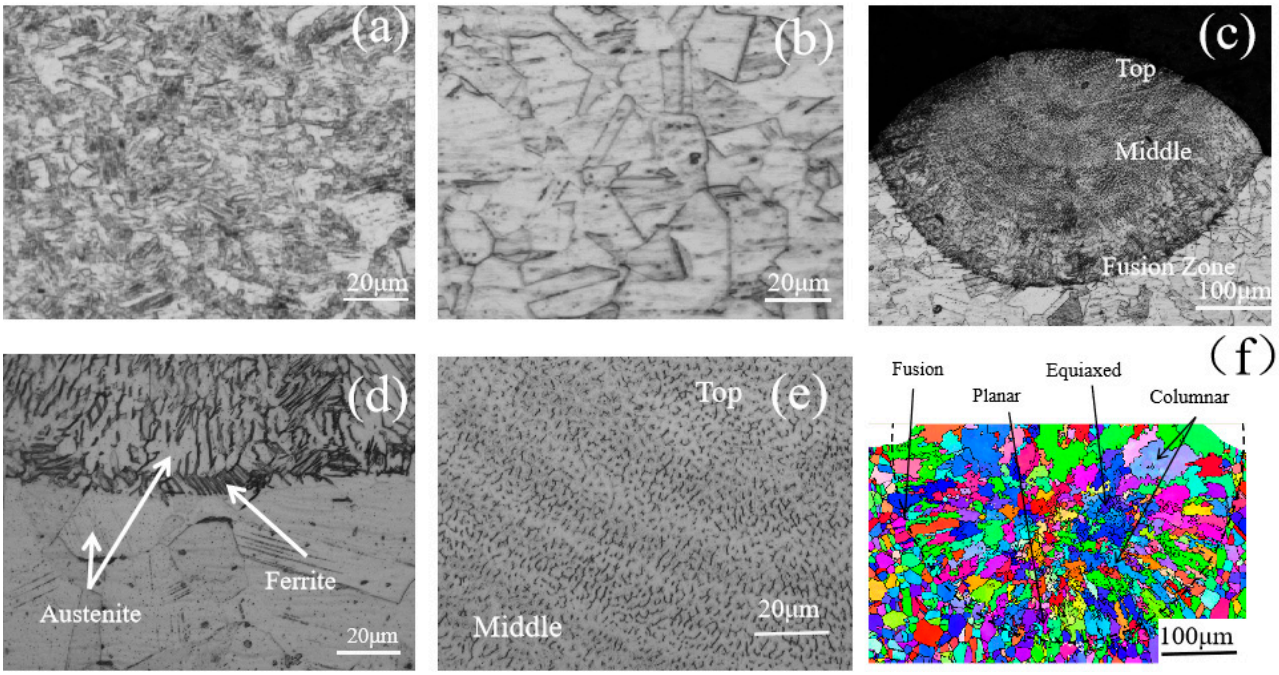

Figure 3. Microstructure of each region in single layer and single channel. (**a**)The original microstructure of the wire (**b**) The original microstructure of the substrate, (**c**) The overall microstructure diagram of the single-layer and single-channel (**d**) The microstructure of the single-layer and single-channel fusion zone (**e**) The microstructure at the top of the wire, (**f**) the EBSD test results of the single-layer and single-channel.

Figure 3c provides an overview of the overall microstructure diagram of a single layer and single channel, with three distinct regions marked in the figure. Moving on to Figure 3d, it displays the microstructure of the single-layer single-channel fusion zone. The heating and cooling of the JHAM process causes changes in grain shape, leading to differences in grain structure between the formed single layer and single channel compared to the substrate. The substrate exhibits coarse cylindrical austenite, while the fusion zone features a close distribution of ferrite, with austenite above the fusion zone. The grains in the fusion zone are smaller than those in the neighboring regions, as the heat generated by the outer surface of the wire in contact with the substrate conducts through the substrate quickly, resulting in solidification before the grains have time to grow.

The larger temperature gradient in the fusion zone compared to other regions promotes grain growth. Moving on to Figure 3e, it illustrates the microstructure at the top of the wire, comprising austenite and a small amount of ferrite. The top of the wire experiences a small temperature gradient, leading to fast crystallization and relatively uniform microstructure distribution. However, slight differences in grain shape exist between the top and middle of the wire due to varying temperature gradients, resulting in different morphologies within the same tissue. Figure 3f displays the EBSD test results, indicating that the grains from the fusion line to the surface layer transition from planar crystal, to columnar crystal, to equiaxed crystal, and finally to columnar crystal again. This grain growth occurs along the direction perpendicular to the fusion line, moving towards the center of the wire. The process occurs because during the crystallization process of the melt pool, the crystal nucleus attaches to the grain surface of the substrate. When the optimal crystallization orientation aligns with the direction of the temperature gradient, the growth progresses from the surface of the wire towards the center of the wire.

Figure 4a depicts the microstructure diagram of a partial section of the single layer and single channel formed using the JHAM method. On the other hand, it is obvious in Figure 4a that the fusion zone is the transition zone between the wire and the substrate, while the heat-affected zone is shown to be different from the grain shapes in the fusion zone by observing the shapes of the grains in the fusion zone. Figure 4b displays the microstructure diagram of the joint passage welded by Li Yusong et al. [18] using the arc fuse additive manufacturing method. A comparison between the two microstructure diagrams reveals that the single layer and single channel formed by the JHAM method exhibit a relatively small heat-affected zone. It is worth noting that different hot working processes have varying degrees of influence on the heat-affected zone of the component.

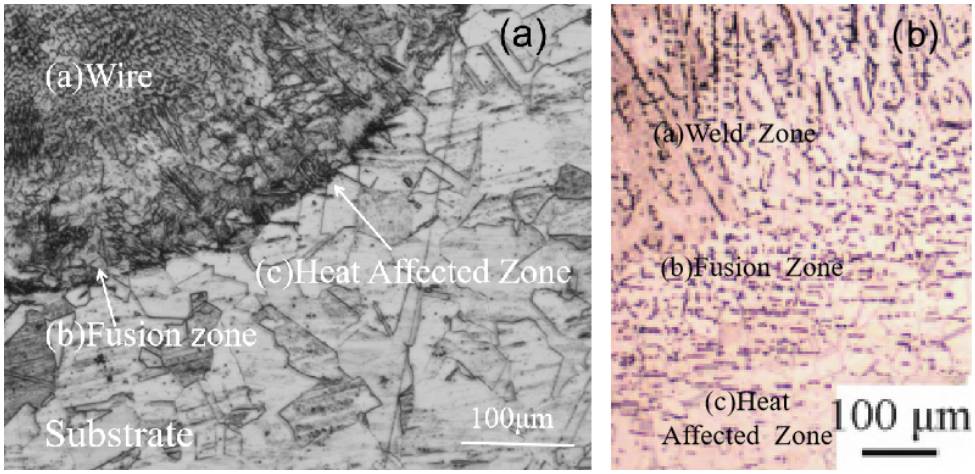

Figure 4. Comparison of heat-affected zone between JHAM (**a**) The microstructure diagram of a partial section of the single layer and single channel formed using the JHAM method and MIG (**b**). The microstructure diagram of the joint passage welded using the arc fuse additive manufacturing method.

3.2. Element Composition and Distribution of Single Layer and Single Channel

To analyze the element composition and content of the single layer and single channel, an energy spectrometer was employed for point scanning on the middle of the wire and the fusion zone. The results of the element content at selected points and their corresponding positions are presented in Figures 5 and 6. The element composition of the printed path layer primarily consists of Fe and Cr, along with other elements. Among these, the Fe element exhibits the highest content, accounting for approximately 60%, followed by a relatively high content of Cr, around 15%. When considering the overall distribution of element content at the three points, it can be observed that compared to the original wire, the middle of the wire shows an increased C content. Conversely, the middle of the wire

and the three points in the fusion zone (i.e., points 1, 2, and 3) exhibit progressively reduced Fe and Cr contents, with a corresponding increase in C content. Furthermore, the content of Cr and Mo elements in the fusion zone increases due to the presence of a small amount of ferrite in the fusion zone, consistent with the concentration of Cr and Mo elements in the ferrite phase, as described by Fan Dongsheng et al. [19]. With the exception of slight segregation of Cr and Mo elements in the fusion zone, the content of other elements in both the middle of the wire and the fusion zone of the single-layer single channel is similar, and the distribution is relatively uniform.

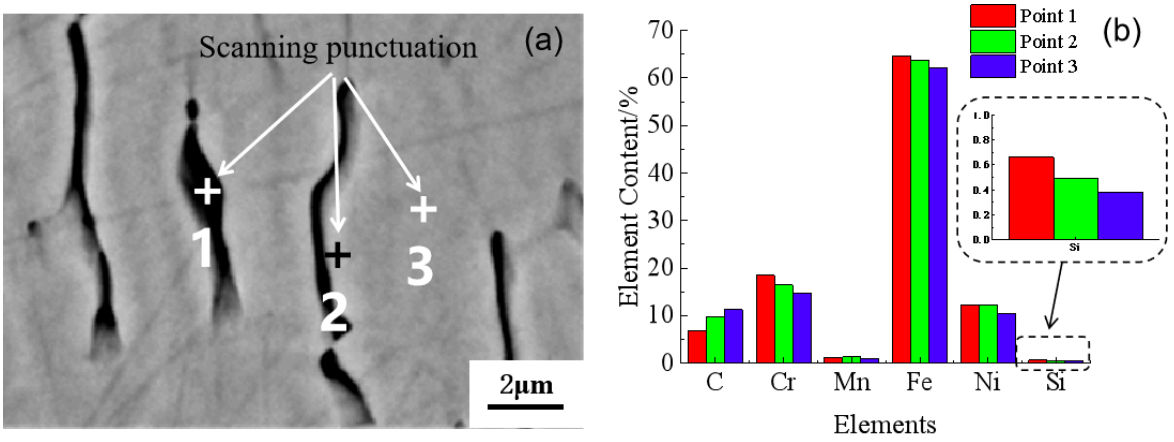

Figure 5. Scanning position (**a**) and element content of EDS point (**b**) in the middle of the wire.

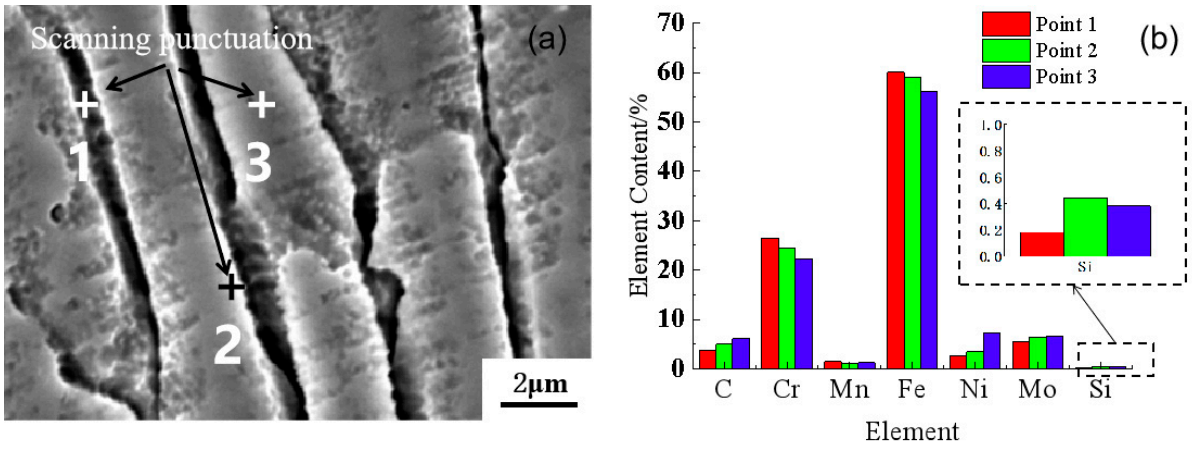

Figure 6. Scanning position (**a**) and element content of EDS point (**b**) in the fusion zone.

3.3. Analysis of Single Layer and Single Channel EBSD Phase Morphology Characteristics

3.3.1. Phase Distribution

The phase composition analysis focuses on the austenitic phase and ferrite phase since the equilibrium structure of austenitic stainless steel typically consists of these two phases [20]. In the EBSD phase distribution diagram of a single layer shown in Figure 7, the dark green color represents the austenite phase, while the yellow color represents the ferritic phase. The results indicate that the volume fraction of austenite content in the tissue reached 99.71%, with very little ferrite content, which was mainly distributed in the fusion zone. An increased proportion of austenite content is beneficial for improving the material's ductility [21].

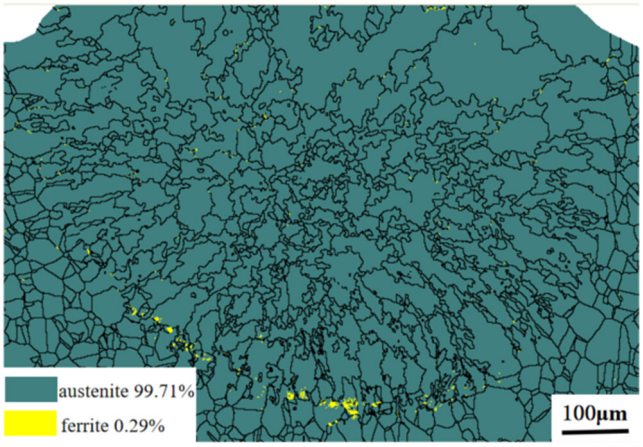

Figure 7. Phase distribution diagram (EBSD) of single layer and single channel.

Additionally, when the phase component of the sample is analyzed by the instrument, because the proportion of other phases is very low, only two phase structures of austenite and ferrite are selected, so when the phase structure of the sample is analyzed by the analysis software, there are no other phases except austenite and ferrite.

3.3.2. Grain Size Distribution

Grain size is a critical factor influencing material properties. Figure 8a presents the overall grain size diagram of a single layer, determined based on the long axis of the fitted ellipse representing the grain's shape. The black lines in the figure are not longitudinal defects, but the color of the lines is subjectively set to black when the image analysis and processing software is used. The corresponding statistical distribution results are displayed in the bar chart in Figure 8b. The horizontal axis represents the grain size, and the vertical axis represents the percentage of different grain sizes. The three marked regions (1), (2), and (3) in Figure 8a represent the fusion zone, the middle of the wire, and the top of the wire, respectively.

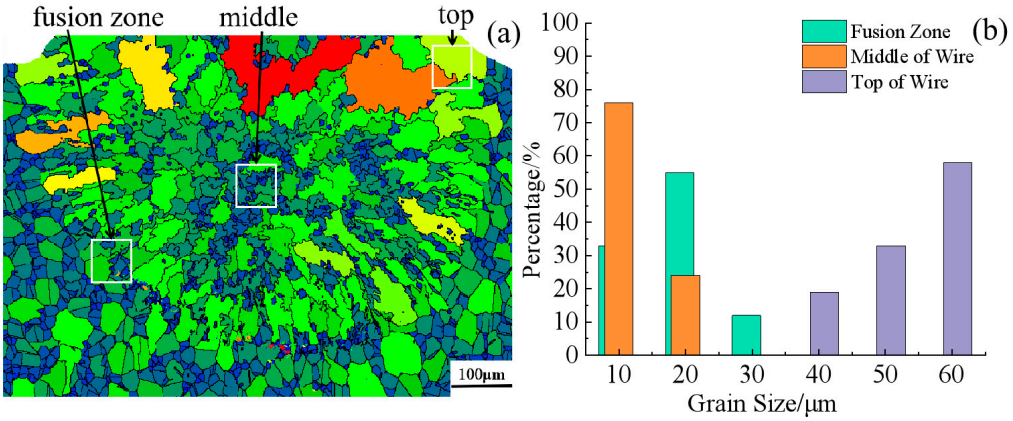

Figure 8. Single-layer and single-channel grain size distribution (**a**) and analysis (**b**).

Based on the statistical results, the grain size in the fusion zone is predominantly around 20 μm, while the grain size is largest at the top of the wire, and relatively smaller (mainly within 10 μm) in the middle of the wire. Grain refinement is advantageous for improving the material's strength. The grains near the fusion zone exhibit smaller columnar crystals and some equiaxed crystals in the plate, while the larger grain size at the top of the wire is due to the large temperature gradient on the outer surface of the wire, which promotes grain growth.

3.3.3. Grain Boundary Angle Distribution

Grain boundaries refer to the interfaces between adjacent grains. They can be categorized based on the angle between the two grains into small-angle grain boundaries ($\theta < 10°$) and large-angle grain boundaries ($\theta > 10°$). The distribution diagram of angular grain boundaries in the single-layer single channel is shown in Figure 9a, with small-angle grain boundaries represented by red lines and large-angle grain boundaries represented by black lines. The statistical results for different regions are presented in Figure 9b.

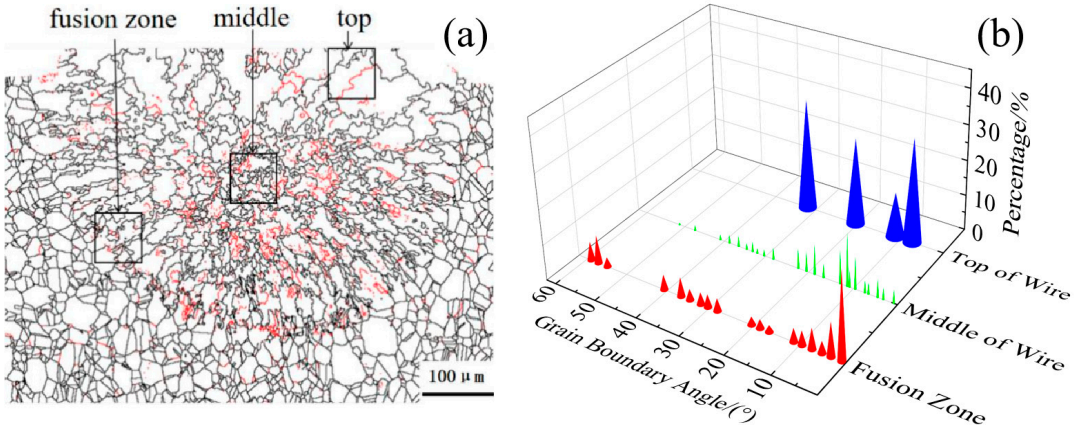

Figure 9. Angle distribution (**a**) and analysis (**b**) of single-layer and single-channel grain boundaries.

The fusion zone and the middle of the wire show a higher proportion of large-angle grain boundaries compared to small-angle grain boundaries, with only slight differences in the number of grain boundaries. The middle of the wire exhibits the highest content of small and medium-angle grain boundaries, which can be attributed to its slower temperature dissipation and higher temperature compared to the other two regions. An increase in temperature leads to a higher content of small-angle grain boundaries and a decrease in large-angle grain boundaries. The presence of small-angle grain boundaries indicates the presence of preferred orientations, which can lead to increased anisotropy. Overall, a higher proportion of large-angle grain boundaries can improve the material's toughness.

Figure 10a is the result of a single-channel, single-layer industrial CT scan with a scanning depth of 12 mm. Figure 10b is a single-layer and single-channel overall three-dimensional transmission scan with a scanning accuracy of 1 μm. It can also be confirmed from the scanning results that there are no longitudinal microcracks such as holes and cracks in the print layer, and if there are any, the scan image will be marked with bright colors.

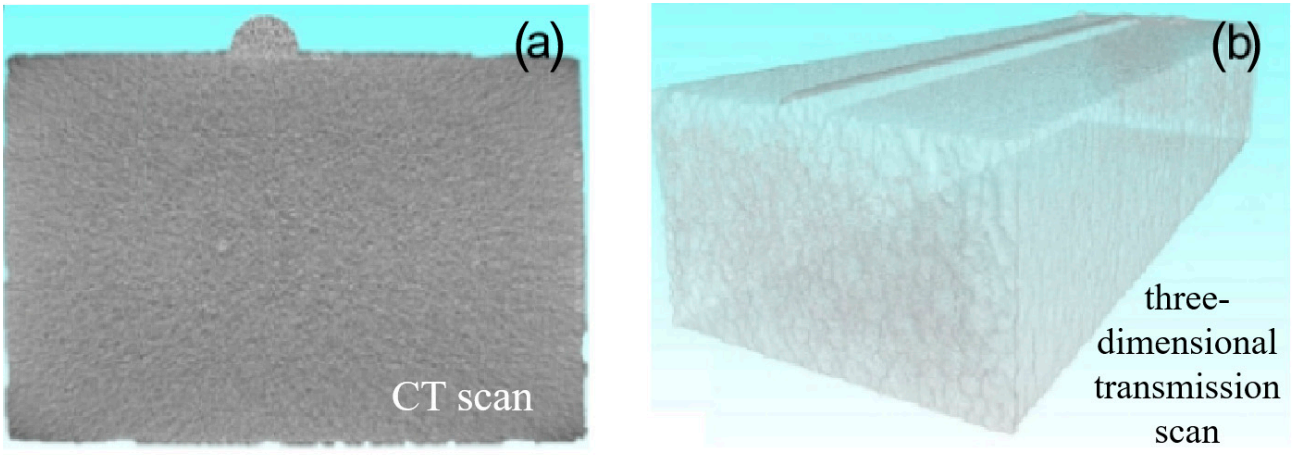

Figure 10. Single-layer and single-channel CT scan (**a**) and three-dimensional transmission scan (**b**).

3.3.4. Distribution of Local Grain Orientation Difference

An analysis of grain orientation difference was conducted to avoid including grain boundary orientation differences. Only orientation differences ranging from 0° to 5° were considered. The distribution diagram of grain orientation difference in the single-layer single channel is shown in Figure 11a. Different colors in the color band represent different sizes of grain orientation differences, with green indicating the minimum value of grain orientation difference. The overall distribution of grain orientation difference in the single-layer single channel shows mostly blue colors, with only a few green areas, indicating relatively small values of grain orientation difference.

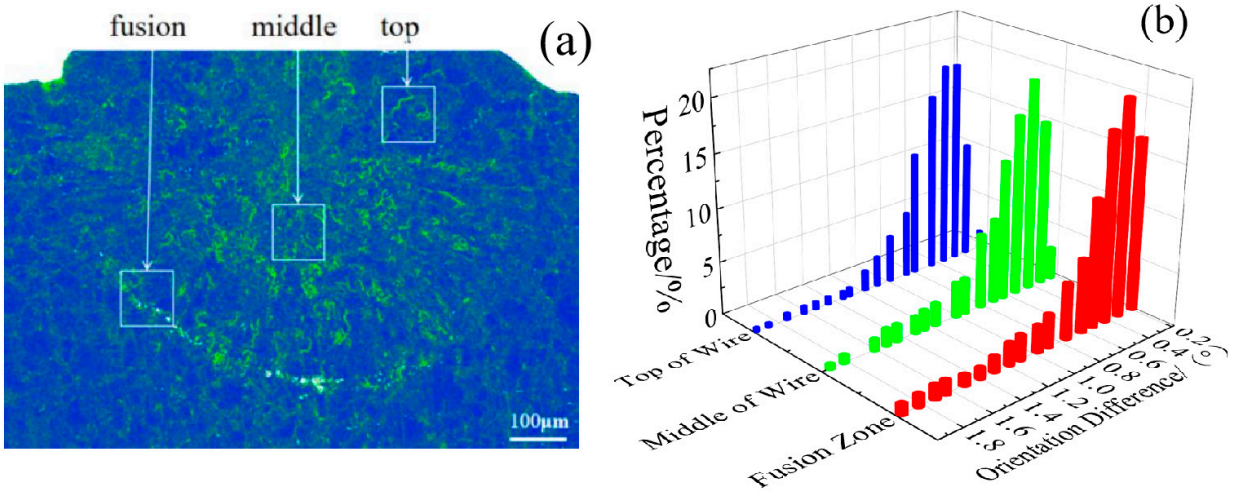

Figure 11. Differential distribution (**a**) and analysis (**b**) of local orientation of single-layer and single-channel grains.

The local orientation difference distribution for the grains in the three regions (fusion zone, middle of the wire, and top of the wire) is depicted in Figure 11b. The distribution of local orientation difference is generally consistent across the three regions, with the highest proportion of orientation differences falling within 1°. An increase in grain orientation difference can lead to a decrease in material strength and plasticity.

Temperature gradient and cooling rate are important factors affecting the local orientation of grain. In terms of temperature gradient, the temperature gradient in Figure 3e directly affects the local orientation difference of grains, and the difference in temperature gradient leads to the difference in grain growth rate, which leads to the difference in grain size and orientation. In terms of cooling rate, the cooling rate of the top of the wire is slower than that of the fusion zone, because the top of the wire is in a vacuum environment, where heat convection is difficult or impossible to produce, resulting in slower heat loss and slower cooling rate. The filament in the fusion zone is in contact with the substrate, and the heat generated can be transferred to the substrate by heat conduction, thus making the cooling rate faster. The difference in cooling rate directly affects the difference in grain size. The faster cooling rate can lead to the formation of fine grains, while the slower cooling rate can lead to the formation of larger grains, resulting in the difference in local grain orientation.

4. Conclusions

In a word, this study focused on analyzing the microstructure of a single-pass monolayer formed with optimal process parameters using various detection methods, leading to the following key findings:

1. The substrate structure consists of coarse columnar austenite, the fusion zone shows a closely distributed ferrite phase, and the area above the fusion zone is predominantly austenite. Notably, there is a significant difference in grain size between the substrate

and the wire. As we move from the fusion line to the top of the wire, the grains transition from planar to columnar, then equiaxed, and finally back to columnar.

2. The microstructure of the single layer is composed of austenite with a small amount of ferrite, where the austenite phase accounts for 99.71% of the content. Apart from Cr and Mo elements, the element content in the middle of the wire and the fusion zone is similar, resulting in a relatively uniform distribution.
3. The grain size in the middle of the wire ranges within 10 μm, with a higher proportion of large-angle grain boundaries, which can improve the material's toughness. The small-angle grain boundary is predominantly distributed in the middle of the wire, leading to an increase in material anisotropy. Additionally, the local orientation difference distribution for the grains in the three regions is consistent, with the highest proportion of orientation differences falling within 1°.

Overall, the analysis of the microstructure using various detection methods provides valuable insights into the characteristics of the single-layer single channel formed with the JHAM method and offers important information for further understanding its properties and potential applications.

Author Contributions: Conceptualization, S.L. and B.L.; methodology, Z.G.; software, J.X.; validation, S.L., Z.G and J.X.; formal analysis, L.Y.; investigation, S.L. and Z.G.; resources, S.L. and B.L.; data curation, Z.G.; writing—original draft preparation, Z.G. and S.L.; writing—review and editing, Z.G. and K.M.; visualization, L.F. and J.C.; supervision, Z.G.; project administration, L.Y.; funding acquisition, S.L. All authors have read and agreed to the published version of the manuscript.

Funding: This research was funded by State Key Laboratory Program (Sklms2021016); 2022 Local Special Scientific Research Project (22JC053); Project of the 14th Five-Year Plan for Education Science in Shaanxi Province in 2021 (SGH21Y0522); 2022 Research Project of Rural Revitalization Research Institute of Shaanxi Vocational Education (22YB020).

Data Availability Statement: The data presented in this study are available in the article.

Conflicts of Interest: The authors declare no conflict of interest.

References

1. Kumar, S.P.; Elangovan, S.; Mohanraj, R.; Ramakrishna, J.R. Review on the evolution and technology of State-of-the-Art metal additive manufacturing processes. *Mater. Today Proc.* **2021**, *46*, 7907–7920. [CrossRef]
2. Lu, B. Additive Manufacturing—Current Situation and Future. *China Mech. Eng.* **2020**, *31*, 19–23.
3. Biegler, M.; Graf, B.; Rethmeier, M. In-situ distortions in LMD additive manufacturing walls can be measured with digital image correlation and predicted using numerical simulations. *Addit. Manuf.* **2018**, *20*, 101–110. [CrossRef]
4. Montoya-Zapata, D.; Creus, C.; Ortizc, I.; Alvarez, P.; Moreno, A.; Posada, J.; Ruiz, O.E. Generation of 2.5D Deposition Strategies for LMD-based Additive Manufacturing. *Procedia Comput. Sci.* **2021**, *180*, 280–289. [CrossRef]
5. Fuchs, J.; Schneider, C.; Enzinger, N. Wire-based additive manufacturing using an electron beam as heat source. *Weld. Word* **2018**, *62*, 267–275. [CrossRef]
6. Panchenko, M.; Maier, G.; Moskvina, V.; Astafurov, S.; Melnikov, E.; Reunova, K.; Kolubaev, E.; Astafurova, E. Microstructure and mechanical properties of Nb-alloyed austenitic CrNi steel fabricated by wire-feed electron beam additive manufacturing. *Mater. Charact.* **2022**, *190*, 112063. [CrossRef]
7. Li, Q.; Wang, G.; Dong, M.; Feng, C.; Luo, Z. Influence of wire compositions on the microstructure and mechanical properties of WAAM Al-Cu aluminum alloy. *Rare Met. Mater. Eng.* **2021**, *50*, 1649–1655.
8. Chen, S.; Yuan, C.; Jiang, F.; Yan, Z.; Zhang, P. Study on Heat Generation Mechanism and Melting Behavior of Droplet Transition in Resistive Heating Metal Wires. *Acta Metall. Sin.* **2018**, *54*, 1297–1310.
9. Li, S.; Ma, K.; Xu, C.; Yang, L.; Lu, B. Numerical Analysis and Experimental Verification of Resistance Additive Manufacturing. *Crystals* **2022**, *12*, 193. [CrossRef]
10. Ma, K.; Li, S.; Xu, C.; Gao, Z.; Yang, L.; Lu, B. Study on the Process Characteristics Based on Joule Heat of Sliding-Pressure Additive Manufacturing. *Materials* **2023**, *16*, 2017. [CrossRef] [PubMed]
11. Guo, T.; Huang, D.; Wang, J.; Li, K.; Sun, Q. Effect of Low-Temperature ECAP with Extended Route and Aging Heat Treatment on Structure and Properties of Cu0.6Cr Alloy. *Rare Met. Mater. Eng.* **2022**, *51*, 3204–3213.
12. Lai, Y.; Ning, L.; Liu, Y.; Liu, N.; Meng, X.; Tan, Z.; Tong, J.; Zheng, Z. Effect of Heat Treatment on Microstructures and Stress Rupture Properties of a Hot-Corrosion Resistant Single Crystal Superalloy. *Rare Met. Mater. Eng.* **2023**, *52*, 2243–2252.
13. Liu, L.; He, Y.; Li, Z.; Zhang, Z. Research on microstructure and mechanical properties of 316 stainless steel fabricated by arc additive manufacturing in different paths. *Trans. China Weld. Inst.* **2020**, *41*, 13–19+97–98.

14. Unnikrishnan, R.; Satish, K.; Ismail, T.; Bhadauria, A.; Shekhawat, S.K.; Khatirkar, R.K.; Sapate, S. Effect of Heat Input on the Microstructure, Residual Stresses and Corrosion Resistance of 304 L Austenitic Stainless Steel Weldments. *Mater. Charact.* **2014**, *93*, 10–23. [CrossRef]
15. Yuan, C.; Chen, S.; Jiang, F.; Yang, F. Electro-thermal-mechanical response analysis of plastic deformation of resistance heating metal wire. *Trans. China Weld. Inst.* **2020**, *41*, 1–6.
16. Asl, H.; Vatani, A. Numerical analysis of the burn-through at in-service welding of 316 stainless steel pipeline. *Int. J. Press. Vessel. Pip.* **2013**, *105*, 49–59. [CrossRef]
17. Nie, D.; Lu, Z.; Zhang, K. Hot bending behavior of SUS 304 stainless steel sheet assisted by resistance heating: Multi-field coupling numerical simulation and experimental investigation. *Int. J. Adv. Manuf. Technol.* **2016**, *87*, 2763–2774. [CrossRef]
18. Li, Y.; Liu, S.; Chang, Z.; Xu, J.; Luo, S.; Li, J. Study on microstructure of 304 stainless steel made by MIG arc additive. *Weld. Technol.* **2023**, *52*, 7–11.
19. Fan, D.; He, C.; Chen, X.; Lian, J. Effect of CO_2 partial pressure on corrosion behavior of 2205 duplex stainless steel in acidic oil and gas fields. *Hot Work. Technol.* **2019**, *48*, 50–55.
20. Zhao, H. *The Effect of Heat Aging on Microstructure and Corrosion Resistance of 316L Stainless Steel Welds*; Xi'an University of Technology: Xi'an, China, 2018.
21. Chen, X.; Li, W.; Ren, P.; Cao, W.; Liu, Q. Effects of C Content on Microstructure and Properties ofFe-Mn-Al-C Low-Density Steels. *Acta Metall. Sin.* **2019**, *55*, 951–957.